中國機械工程學刊第四十五卷第五期第 489~499 頁(民國一百一十三年)
Journal of the Chinese Society of Mechanical Engineers, Vol.45, No.5, pp489~499 (2024)

Thermo-fluid Dynamics of Melt Pools in Laser Powder Bed Fusion of Scalmalloy®: CFD Simulations, Non-dimensional Analysis, and Microstructure Prediction

Zaki S. Saldi*, Arief S. Budiman**, Fergyanto E. Gunawan***and Tim Pasang****

Keywords：CFD, LPBF, melt pool, microstructure.

ABSTRACT

In this work, thermo-fluid dynamics of melt pools formed during Laser Powder Bed Fusion (LPBF) of a Scalmalloy® part was studied using Computational Fluid Dynamics (CFD) simulations. The formation of the melt pools was examined, and non-dimensional analysis of various flow and heat transfer driving forces was performed to justify the assumptions used in the model. The microstructure model predicted that the morphology factors increase with the energy density, due to thermocapillary effect and decreasing cooling rates. At high energy density the grain morphology tends to be columnar rather than equiaxed, albeit with the existence of mixed columnar-equiaxed regime, which is confirmed by the evaluation of the solidification map. In addition, the microstructure grain size was predicted to decrease with the scanning speed, as the cooling rate intensifies.

Paper Received December, 2023. Revised February, 2024. Accepted February, 2024. Author for Correspondence: Zaki S. Saldi.

* *Assistant Professor, Department of Product Design, Universitas Pembangunan Jaya, Tangerang Selatan, 15413, Indonesia.*

Center for Urban Studies, Universitas Pembangunan Jaya, Tangerang Selatan, 15413, Indonesia.

** *Assistant Professor, Department of Manufacturing and Mechanical Engineering and Technology, Oregon Institute of Technology, Klamath Falls, 97601, OR, USA*

Oregon Renewable Energy Center (OREC), Klamath Falls, 97601, OR, USA

*** *Professor, Industrial Engineering Department, BINUS Graduate Program - Master of Industrial Engineering, Bina Nusantara University, Jakarta, 11480, Indonesia*

**** *Professor, Department of Engineering Design, Manufacturing and Management Systems, Western Michigan University, Kalamazoo, 4900-5200, MI, USA*

INTRODUCTION

Metal Additive Manufacturing (MAM) technologies are gaining traction in manufacturing industries due to their ability to rapidly produce high-quality metallic 3D components layer by layer. Compared to conventional subtractive methods and forming processes, MAM offers distinct advantages, including the ability to create complex shapes with features such as overhangs and lattice structures that are difficult or expensive to obtain otherwise. These structures are highly sought after for their functional superiority, providing high strength-to-weight performance and design flexibility.

Among the existing MAM processes, Laser-Powder Bed Fusion (LPBF) has found applications in various industries, including aerospace (Blakey-Milner et al., 2021), maritime (Ziolkowski and Dyl., 2020), automotive (Vasco, 2021), medical (Huang et al., 2020), and energy systems (Sireesha et al., 2018). LPBF enables the fabrication of parts using a wide range of metallic materials, including alloys based on Fe, Al, Ti, Ni, Cu, Co, and composite metals (Gokuldoss et al., 2017). Previous studies have demonstrated that LPBF applied to structurally optimized aviation components can result in a weight reduction of approximately 33% without compromising mechanical strength (Wang et al., 2022). Lightweight components incorporating lattice structures based on tessellation can be built using LPBF, allowing tuning of mechanical properties to obtain better structural performance (Bhat et al., 2023a; Bhat et al., 2023b). Treatment using LPBF was also demonstrated to recover the corrosion resistance of alloy metal (Lee & Liu, 2018).

Despite its advantages, LPBF still faces several challenges. The rapid local heating and solidification, accompanied by high temperature gradients in multiple directions during the layer-by-layer thermal cycles, result in microstructure non-uniformity, residual stress, part distortion, and compromised

mechanical properties as well as surface quality (Shaikh et al., 2022). Poor local mechanical properties arise due to porosity formation (Khairallah et al., 2016), residual stresses (Shaikh et al., 2022), cracking, and distortion (Parimi et al., 2014). LPBF parts can also experience significant elongation, reaching up to 10.1% (Wen et al., 2018), which poses challenges for engineering structures.

In the context of LPBF, one popular material currently utilized is Scalmalloy®, an alloy combining scandium, aluminum, and magnesium. Scalmalloy® stands out among other aluminum alloys due to its ability to overcome hot cracking issues commonly encountered in high-temperature processes. This is attributed to the formation of nucleation sites at elevated temperatures, which are well distributed in the solidified microstructure. The addition of at least 0.6 wt% Sc in the alloy leads to the formation of Al-Sc precipitates, further promoting nucleation site formation (Kuo et al., 2021). These precipitates effectively limit the formation of columnar grains that typically trigger hot cracking mechanisms.

Despite ongoing experimental efforts to study the post-solidification microstructure of LPBF-printed Scalmalloy® materials, questions remain regarding the formation of a bi-modal grain morphology distribution in the melt pool, characterized by the coexistence of fine equiaxed grains and coarse columnar grains (Martucci et al., 2022). To this end, there is still a gap with regards to understanding how heat transfer and fluid flows within the melt pool for a given set of process parameters contribute to the grain distribution in the microstructure of of LPBF-printed Scalmalloy® and its correlation with the mechanical properties of the final parts. The work in this paper attempted to fill this gap, so that it can later guide the process parameters optimization for LPBF of Scalmalloy® parts through a combination of numerical simulations and experiments. In line with this direction, a numerical model pertaining to the thermo-fluid dynamics of melt pools formed during LPBF of Scalmalloy® has been developed in this work. Additionally, the microstructure was evaluated to study how different energy densities influence the morphology distribution in Scalmalloy® parts during the LPBF process.

PROBLEM OF INTEREST

The problem of interest in this work is the LPBF of a Scalmalloy® workpiece, as illustrated in Fig.1. This setup is based on previous experiment (Turangi et al., 2020), in which the energy density range of 40-110 J/mm^3 resulted in Scalmalloy® parts with relative densities over 99%. The dimension of the workpiece is 50 mm × 10 mm × 2.5 mm, in x, y, and z, respectively.

A powder bed with a thickness of 30 microns was deposited on top of the sample. LPBF proceeds through the translation of a laser beam that melts the powder, resulting in a melt pool, fusing it with the base material during solidification. A Renishaw AM 400 SLM machine was used to deliver a pulsed laser with a focus diameter of 70 microns and a maximum power of 400 W. The hatch distance of the laser scan is 150 microns. Other important process parameters are laser scanning speed and energy density. The energy density E_d is a function of laser scanning speed v_l, which can be formulated as (Spierings et al, 2017):

$$E_d = \frac{P}{v_l D_h t_l} \tag{1}$$

where P is the laser power, D_h the hatch distance, and t_l the layer thickness. In this work, E_d was varied by using several values of scanning speed. The process parameter variation is summarized in Table 1, where energy density is inversely proportional to laser scanning speed, according to Equation (1). The energy densities of 64 and 80 J/mm^3 were selected based on the range in the reference experiment. The highest value (160 J/mm^3) lies outside the range but was chosen to represent a high energy density scenario.

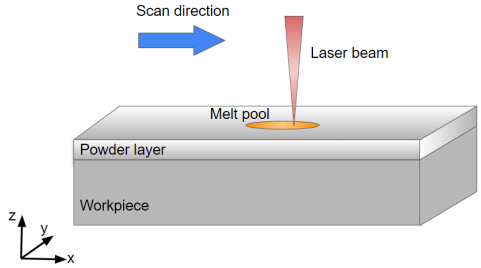

Fig. 1. The schematic of LPBF of Scalmalloy®. The laser scans in x-direction (from left to right).

Table 1. Parameter variation used in this study. (ED in the left column stands for energy density)

Case Name	Energy density (J/mm^3)	Scanning speed (mm/s)
ED160	160	555
ED080	80	1111
ED064	64	1389

The composition of Scalmalloy® powder used (Turangi et al., 2020) by analysis was as follows: Al (bal.), Mg (4.55 wt%), Sc (0.65 wt%), Zr (0.3 wt%), Mn (0.51 wt%), Si (0.16 wt%), Fe (0.14 wt%), Zn (0.02 wt%), Ti (0.01 wt%), Cu (0.01 wt%), V (0.01 wt%), and O (0.02 wt%). The examination of powder morphology showed that the maximum particle diameter is 63 microns, and 6 vol% particles were smaller than 20 microns.

SIMULATION MODEL

CFD Governing Equations

The mathematical model for the simulation employs the following assumptions: (1) The fluid flow

in the melt pool is continuum, Newtonian, incompressible, and laminar; (2) The powder layer follows a continuum behaviour with effective thermo-physical properties; (3) The melt pool surface is flat and non-deformable; (4) The evaporative mass loss is neglected.

The model is represented by the following governing equations of conservation of mass (continuity), momentum (Navier-Stokes), and energy, respectively.

$$\frac{\partial \rho}{\partial t} + \nabla \cdot (\rho \vec{U}) = 0 \tag{2}$$

$$\frac{\partial}{\partial t}(\rho \vec{U}) + \nabla \cdot (\rho \vec{U}\vec{U}) = -\nabla p + \nabla \cdot (\mu \nabla \vec{U}) + \vec{S}_g + \vec{S}_m \tag{3}$$

$$\frac{\partial}{\partial t}(\rho H) + \nabla \cdot \left(\rho \vec{U} H\right) = \nabla \cdot (k \nabla T) + S_H \tag{4}$$

In the above equations, ρ is density, $\vec{U}$ velocity vector, p pressure, μ dynamic viscosity, $\vec{S}_g$ and $\vec{S}_m$ momentum source terms, H total enthalpy, k thermal conductivity, T temperature, and S_H energy source term.

In the Navier-Stokes equation, the two body forces $\vec{S}_g$and $\vec{S}_m$ represent thermal buoyancy effects and momentum damping in the mushy zone ($0 \leq \alpha \leq 1$, α being the liquid fraction), respectively. The thermal buoyancy force is expressed as

$$\vec{S}_g = \rho \vec{g}\left[1 - \beta\left(T - T_{ref}\right)\right] \tag{5}$$

where $\vec{g}$ is the gravity acceleration vector, β thermal expansion coefficient, and T_{ref} reference temperature.

The mushy zone damping force is formulated as

$$\vec{S}_m = -C\frac{(1-\alpha)^2}{(\alpha^3 + \epsilon)}\vec{U} \tag{6}$$

Here, C is the velocity damping coefficient, set as 10^6, which is active in the solid zone (where liquid fraction α = 0). The constant ϵ is a very small number (set as 10^{-5}) to avoid division by zero in the solid zone.

The energy source term represents the volumetric heat source due to energy transfer from the laser into the powder layer and the sample, which is defined in a volumetric Gaussian form, as follow:

$$S_H = \frac{3\eta P}{h_l \pi r_l^2}\left[\frac{-3[(x - x_i - v_l t)^2 + (y - y_i)^2]}{r_l^2}\right] \exp\left[\frac{z^2}{h_l^2}\right] \tag{7}$$

where η is the laser absorptivity by the metal powder, r_l laser beam radius, and h_l the laser penetration depth. The latter can be approximated based on the powder layer thickness and laser absorptivity (Rahman et al., 2020), i.e.

$$h_l = \frac{t_l}{2.303\eta} \tag{8}$$

In addition, x, y, and z are the computational cell coordinates, whereas x_i and y_i are the initial laser position coordinates.

The physics of phase change (melting and solidification) is considered by defining the total enthalpy in energy equation as the sum of sensible enthalpy and phase change (melting) enthalpy, where the latter depends on the liquid fraction $\alpha(T)$, as follow:

$$H(T) = h + \Delta H_m = \int_{T_0}^{T} C_p(T)dT + L\alpha(T) \tag{9}$$

where L is the latent heat of fusion. The liquid fraction is assumed to vary linearly with temperature between the solidus (T_s) and liquidus temperature (T_l).

In the present work, CFD software ANSYS Fluent 2020R2 with User-Defined Function (UDF) was employed.

Computational Domain and Boundary Conditions

In many cases, the melt pool is symmetrical with respect to the plane along the laser scan direction. With this symmetry assumption, the computational domain only covers half of the melt pool, and thus the symmetry boundary condition was imposed, as shown in Fig.2.

At the bottom and three side boundaries, the no-slip velocity ($\vec{U} = 0$) and thermally insulated conditions ($dT/dn = 0$, with n the normal direction of the boundary) were imposed. At the top boundary, flat surface assumption implies that $u_z = 0$. Moreover, there is a balance between the shear force and the surface tension (Marangoni condition):

$$\tau_{xz} = -\mu\left(\frac{\partial u_x}{\partial z}\right)_{top} = \frac{d\sigma}{dT}\left(\frac{\partial T}{\partial x}\right)_{top} \tag{10}$$

$$\tau_{yz} = -\mu\left(\frac{\partial u_y}{\partial z}\right)_{top} = \frac{d\sigma}{dT}\left(\frac{\partial T}{\partial y}\right)_{top} \tag{11}$$

where $d\sigma/dT$ is the temperature gradient of surface tension. Additionally, heat losses corresponding with convection, radiation, and evaporation were also imposed at the top boundary:

$$k\left(\frac{\partial T}{\partial z}\right)_{top} = -h_c\left(T - T_{ref}\right) - \sigma_B \varepsilon_r\left(T^4 - T_{ref}^4\right) - \varphi L_v p_{atm}\sqrt{\frac{m_A}{2\pi k_B T}}\, exp\left[\frac{L_v m_A (T - T_b)}{k_B T T_b}\right] \tag{12}$$

In equation (12), h_c is the convective heat transfer coefficient, σ_B the Stefan-Boltzmann constant, ε_r surface emissivity, φ evaporation coefficient, L_v latent heat of vaporization, p_{atm} atmospheric pressure, m_A atomic mass, k_B Boltzmann constant, and T_b boiling temperature.

The computational domain was spatially discretized into a finite number of computational cells (mesh), where high mesh resolution was concentrated in the melt pool region along the laser path. Mesh independence study was performed to evaluate the sensitivity of the numerical solution to the refinement of the mesh. It was found that the mesh independent

solution was obtained using around 2 million computational cells with refinement in the melt pool, corresponding with the smallest element of 0.5 microns.

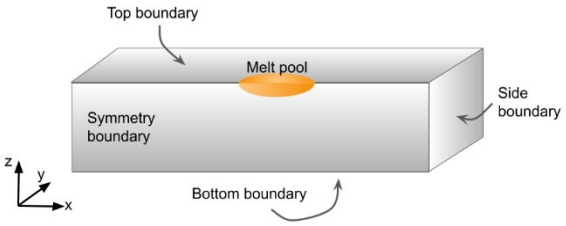

Fig. 2. Computational domain and boundaries used in the simulation.

Thermophysical Properties and Process Parameters

The thermophysical properties of Scalmalloy® and the process parameters used in the simulation are outlined in Table 2. It must be noted that although some parameters are clearly described in literature and/or material database, some others were approximated or assumed due to lack of data. For example, laser absorptivity of the powder bed was estimated as the value for pure spherical aluminum powder bed and a substrate (Boley et al., 2015), instead of for Scalmalloy® powder with the given composition. Another example is the powder bed porosity, which was approximated using the volume ratio of a pack of spheres with uniform size that can fit within the total volume of the bed (length × width × layer thickness). The estimated value (ϕ =0.48) lies within the typical range found in literature.

The bulk properties, including density, thermal conductivity, and specific heat, were especially treated by accounting for the phase values (solid and liquid, as listed in Table 2), which are weighted by the liquid fraction. Additionally, porosity was also considered in the calculation of the bulk properties. Here, the solid substrate positioned below the powder bed has zero porosity. The following expressions were used to update the properties at each time step:

$$\rho = \phi\rho_a + (1-\phi)[\alpha\rho_l + (1-\alpha)\rho_s] \quad (13)$$

$$C_p = [\alpha\rho_l C_{pl} + (1-\alpha)\rho_s C_{ps}]/\rho \quad (14)$$

$$k = \phi k_a + (1-\phi)[\alpha k_l + (1-\alpha)k_s] \quad (15)$$

In the simulation, the laser movement was set in the x-direction, from its initial position at x = 2.2 mm to its final position at x = 2.8 mm, hence with a traveling distance of 0.6 mm.

Numerical Settings

The conservation equations were discretized using the finite volume method. Spatial discretization for the convective terms was based on the 2nd-order upwind scheme, whereas 1st-order implicit Euler scheme was used for the transient terms. A time step size of 10^{-6} s was employed, with a maximum iteration of 50 per time step. Under-relaxation factor of 0.3 was used for pressure, 0.7 for velocity vectors, 0.9 for liquid fraction update, and 0.8 for energy. A convergence criterion of 10^{-6} was used for the residual of the system of linear equation iteration to obtain velocity vectors, and 10^{-7} for energy. The pressure-velocity coupling was treated using the SIMPLE algorithm.

Table 2. Thermophysical properties of Scalmalloy® and process parameters used in the simulation.

Properties	Symbol	Values
Density (solid)	ρ_s	2670 kg m^{-3}
Density (liquid)	ρ	2580 kg m^{-3}
Thermal conductivity (solid)	k_s	100 W m^{-1} K
Thermal conductivity (liquid)	k_1	120 W m^{-1} K^{-}
Specific heat capacity (solid)	C_{ps}	935 J kg^{-1} K^{-1}
Specific heat capacity (liquid)	C_{p1}	1073 J kg^{-1} K
Latent heat of fusion	L	3.86×10^{-5} J
Solidus temperature	T_5	873 K
Liquidus temperature	T_1	908 K
Dynamic viscosity	μ	1.38×10^{-3} kg
Thermal expansion coefficient	β	1.8×10^{-5} K^{-1}
Temperature gradient of surface tension	$d\sigma/dT$	-3.5×10^{-4} N
Reference	T_{ref}	300 K
Convective heat transfer coefficient	h_{c}	10 W m^{-2} K^{-1}
Surface emissivity	ε_{r}	0.2
Evaporation coefficient	φ	0.82
Latent heat of vaporization	L_{v}	2.84×10^5 J
Atomic mass	m_A	0.02738 kg
Boiling temperature	T_b	2800 K
Laser power	P	400 W
Laser beam radius	r_{l}	35 microns
Laser absorptivity	η	0.22
Laser penetration depth	h_{l}	59.21
Powder bed porosity	ϕ	0.48

Microstructure Prediction Model

One of the main interests in the LPBF study is to evaluate how the energy transfer from the laser source affects the thermo-fluid dynamics of the melt pool and eventually the microstructure characteristics of the sample. CFD results can be used as inputs to a predictive model for the microstructure. The following important variables were obtained from CFD simulations and used in the microstructure model (Raghavan et al., 2016; Bayat et al., 2019), i.e.

temperature gradient, cooling rate, growth velocity, and grain morphology factor.

The temperature gradient components in three directions can be directly obtained from simulations:

$$\vec{G} = [G_x\ , G_y\ , G_z] = \left[\frac{\partial T}{\partial x}\ , \frac{\partial T}{\partial y}\ , \frac{\partial T}{\partial z}\right] \quad (16)$$

The cooling rate can be calculated as:

$$CR = \frac{T_l - T_s}{t_l - t_s} \quad (17)$$

where t_l and t_s are time taken to reach liquidus and solidus temperature, respectively. The morphology factor can be estimated using:

$$F = \frac{G}{R} \quad (18)$$

where the growth rate R is calculated as:

$$R = \frac{CR}{G} \quad (19)$$

Two possible microstructures resulting from the process are columnar and equiaxed grains, which depend on the grain morphology factor. High morphology factor usually results in columnar grains, whereas low values result in equiaxed grains. Equiaxed structures are usually preferred to columnar ones since they promote isotropy, hence loading direction flexibility of the final manufactured parts. Furthermore, the grain size can also be deduced from the cooling rate, i.e. the product of temperature gradient and growth rate (Equation (19)). The higher the cooling rate, the smaller the grain size. Small grains are associated with better mechanical properties, e.g. hardness, yield strength (Hall-Petch strengthening (Thangaraju et al., 2012)), and creep resistance. In this work, the effect of process parameters (Table 1) on the grain morphology was studied.

RESULTS AND DISCUSSIONS

Melt Pool Size

The melt pool formed by melting of the powder bed and substrate due to laser irradiation is shown in Fig.3 for the three cases simulated. The melt pools shown correspond with the quasi-steady state, where it is assumed that the rate of change of melt pool shape, temperature profile, and velocity profile are already negligibly small, despite the continuing translation of the laser beam. It is obvious that the size of the melt pool (volume, length, width, and depth) increases with the energy density. At the highest energy density (ED160), the scanning speed is the lowest, such that the rate of laser energy absorbed into the substrate is high, causing higher peak temperature at the melt pool center, as summarized in Table 3.

It is also shown in Fig.3 that the melt pool surface flow is radially outward for all cases studied. The outward flow from the melt pool center at high temperature to the melt pool edge at lower temperature can be attributed to the thermocapillary (Marangoni) effect due to gradient of surface tension with respect to temperature, $d\sigma/dT$. As shown in Table 2, $d\sigma/dT$ is negative. This implies that surface tension decreases with temperature, and surface tension at the melt pool center is lower than that at the edge. Consequently, the flow direction is from the center, i.e. area with low surface tension, to the edge (with high surface tension). This in turn extends the melt pool boundary (illustrated as the solidus and liquidus temperature isolines in Fig.3) radially. With the high temperature gradient in ED160 case, the Marangoni effect was the strongest, causing higher convective heat transfer, hence larger melt pool. The maximum velocity magnitude in Table 3 also increases with the energy density, indicating higher convection at low laser scanning speed. Due to continuity, at the melt pool edge the surface flow is deflected by the solid boundary towards z-direction. With stronger convective flow in a high energy density case, the flow velocity in this direction is also higher, such that the melt boundary is also pushed further downward, resulting in a deeper melt pool. The melt pool size (volume and dimension in three directions) is also summarized in Table 4. The range of melt pool depth obtained from simulations (~51 - 63 microns) agrees well with the laser penetration depth in Table 2 (59.21 microns).

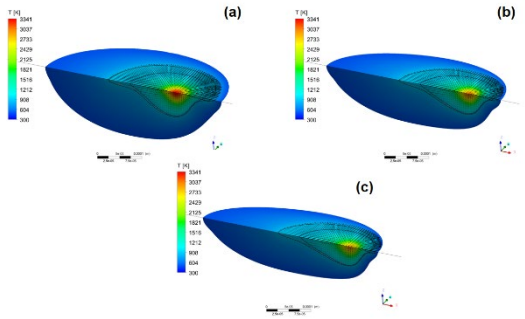

Fig. 3. Temperature fields and velocity vectors in the melt pool at quasi-steady state: (a) ED160; (b) ED080; and (c) ED064.

Table 3. Maximum velocity magnitude and maximum temperature of the melt pool with varying energy density at quasi-steady state.

Case	v_{max}(m/s)	T(K)
ED160	5.45	3341.41
ED080	5.41	3038.55
ED064	5.32	2883.13

Table 4. Size of the melt pool with varying energy density.

Case	Volume (mm^3)	Length (mm)	Depth (mm)	Half-width (mm)
ED160	3.6×10^{-4}	0.26	0.0628	0.118
ED080	2.54×10^{-4}	0.24	0.0542	0.0965
ED064	2.23×10^{-4}	0.23	0.051	0.0863

The sequence to quasi-steady state can be explained in Fig.4, showing the time history of maximum temperature and volume of the melt pool. As all three cases use the same laser traveling distance, the time needed to reach the final laser position (end of simulation) is the shortest for ED064 case, since it corresponds with the highest scanning speed.

The trend observed in Fig.3 that maximum temperature and melt pool volume increase with energy density is also demonstrated in Fig.4. In all three cases, a steep increase of maximum temperature and melt pool volume is observed initially, and their rates of change decrease towards the quasi-steady state. The time needed to reach quasi-steady state also increases with the energy density, due to longer interaction time between laser and the larger melt pool at low scanning speed.

In LPBF with high energy density, the high temperature of the melt pool will also lower the reflectivity of the powder bed, thus increasing its laser absorptivity (Khorasani et al., 2022). This may lead to a deeper melt pool, and even transition to keyhole mode at sufficiently high temperature. Based on this notion, it is important to revisit the laser absorptivity currently used by varying its value with the energy density in the future work to enhance the prediction of the melt pool characteristics.

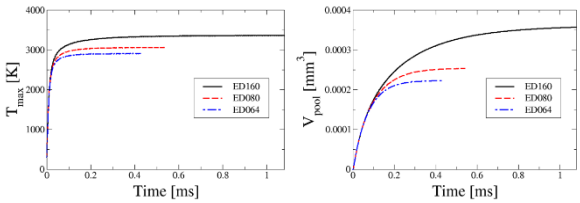

(a) (b)

Fig. 4. Time history of (a) Maximum temperature; and (b) Melt pool volume.

Non-dimensional Number Analysis

Melt pool formed during heat-intensive material processing involves a wide range of physical phenomena. It is widely known that there are several factors that contribute to the fluid flow and heat transfer in the melt pool and to the surrounding solid substrate or the heat-affected zone. The importance of the driving forces can be assessed using a simple, yet powerful method based on non-dimensional numbers. In this subsection, several important non-dimensional numbers pertaining to the melt pool obtained from the simulation are evaluated to gain insights into the interplay between various possible driving forces of the flow in the range of process parameters employed in the current study. Additionally, the non-dimensional numbers are also useful in evaluating the validity of assumptions employed in the model and simulations. These numbers were calculated at the quasi-steady state and are outlined in Table 5.

It is known that the main driving force of the melt pool flow is thermocapillary force or Marangoni effect, due to surface tension gradients that result from temperature gradient at the pool surface. At the surface, due to the tendency of a liquid to resist shear, viscous effects are also present. The ratio of thermocapillary force to the viscous force can be characterized using the Marangoni number, Ma:

$$\mathrm{Ma} = \frac{\rho L_c \left(\frac{d\sigma}{dT}\right) \Delta T_{max}}{\mu^2} \tag{22}$$

where L_c is the melt pool characteristic length, taken as the radius or half-width of the pool, and ΔT_{max} is the maximum temperature difference. From Table 5, it can be seen that Ma is in the order of 10^4 to 10^5 or Ma >> 1 for all the cases studied. This suggests that thermocapillary effect is considerably more dominant than viscous effect.

Table 5. Non-dimensional numbers of the quasi-steady melt pool obtained from simulations.

Case	Ma	Pe	Gr	We	Re
ED160	1.4×10^5	14.86	0.0397	10.05	1200
ED080	1.01×10^5	12.02	0.019	8.1	974
ED064	8.37×10^4	10.61	0.0127	7	860

The next important non-dimensional number is Péclet number, formulated as

$$\mathrm{Pe} = \frac{\rho C_p v L_c}{k} \tag{23}$$

which represents the ratio of convective to conductive heat transfer. The predicted Pe in Table 5 suggests that heat convection in the melt pool outweighs heat conduction by the factor of 10 - 15. This has an important consequence in terms of melt pool thermal field prediction using numerical simulations in that one cannot neglect the fluid flows in the pool or simply rely on a solid conduction model.

Beside thermocapillary and viscous forces, buoyancy force is also present in the melt pool due to temperature difference in the direction normal to the laser scan direction. The temperature difference thus gives rise to the density difference that can also drive the flow, i.e the natural convection mode. The ratio of buoyancy to viscous force is represented by Grashof number, Gr

$$\mathrm{Gr} = \frac{g\beta\rho^2 L_b^3 \Delta T}{\mu^2} \tag{24}$$

where L_b is the buoyancy characteristic length and defined as one forth of the melt pool radius. However, it is obvious from Table 5 that Gr is only of the order of 10^{-2}, which implies that buoyancy force is much less significant than viscous force. Such a characteristic is also caused by the very small dimension of the melt pool, hence much less important body force. By considering both Ma and Gr, it can be easily predicted that the ratio of thermocapillary to buoyancy effects is $\mathrm{Ma/Gr} \approx 10^6 - 10^7$. Therefore, it is clearly proven that thermocapillary (Marangoni) effect is the most significant in driving the melt pool flow.

The simulations were performed based on a model that assumes a non-deformable melt pool surface, or in other words, a flat melt pool surface. The validity of such assumption can be tested using the Weber number, We, i.e., the ratio of inertia to surface forces:

$$\mathrm{We} = \frac{\rho v^2 L_c}{\sigma_0} \qquad (25)$$

where σ_0 is the surface tension. For sufficiently low We, either at very low velocity or very high surface tension, the surface is kept at the minimum area possible, hence the tendency to flatten instead of to deform. Therefore, the free surface deformation can be neglected and the flat surface assumption in the numerical model has a strong rationale. However, this is not the case observed from simulations, as outlined in Table 5, where We is predicted to be in the range of 7 – 10 for all the cases evaluated. This implies that a more suitable model incorporating free surface deformation is needed.

Furthermore, the laminar flow assumption can be evaluated using the Reynolds number, Re, which defines the ratio of inertial force to viscous force.

$$\mathrm{Re} = \frac{\rho v L_c}{\mu} \qquad (26)$$

It was suggested that melt pool flow in the laser welding process is turbulent for Re > 600 (Atthey, 1980). It was also experimentally demonstrated that melt pool flows in additive manufacturing exhibit randomness, which characterizes turbulence (Wirth et al., 2018). The predicted Re in the current study lies in the range of 860 - 1200. Based on this, it can be argued that the assumption of laminar flow used in the current simulations may need to be revisited, and comparison with simulations using turbulence models should be employed in future works. With a turbulence model, one can expect to capture the effect of local velocity fluctuations to the overall momentum transport and heat transfer.

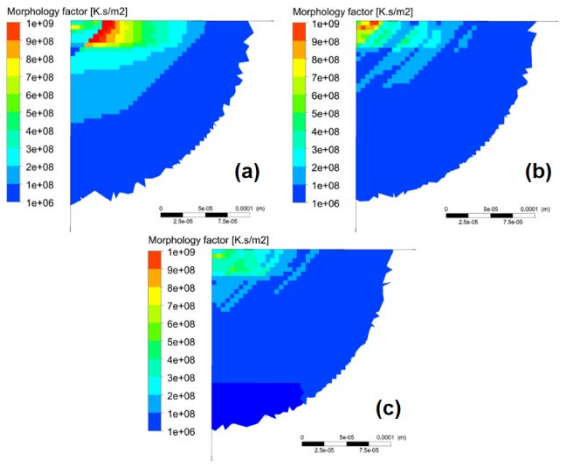

Fig. 5. Cell values of morphology factor at cross section just behind the melt pool: (a) ED160; (b) ED080; and (c) ED064.

Microstructure Prediction

From the numerical simulations, the several variables can be extracted and/or calculated for all computational elements to evaluate the microstructure characteristics of the printed layer with the given process parameters. First, the morphology factor in the solidified region can be evaluated and compared for different energy density or laser scanning speed.

Table 6. Plane-averaged values of morphology factor.

Case	x-coordinate of YZ plane (mm)	F_{avg} (Ks m^{-2})
ED160	2.625	1.26×10^8
ED080	2.617	6.93×10^7
ED064	2.611	5.84×10^7

The cell values of morphology factor at the sample plane are shown in Fig.5 for the three studied cases. At high energy density (ED160), a region of high morphology factor ($\sim 10^9$) was obtained close to the surface. The area of high morphology factor was significantly reduced for ED080 case. In ED064 case, the maximum morphology factor is only $\sim 7 \times 10^8$. The plane-averaged values of morphology factor are summarized in Table 6. From both Fig.5 and Table 6, the maximum and averaged morphology factor increases with the energy density, hence inversely proportional to the laser scanning speed.

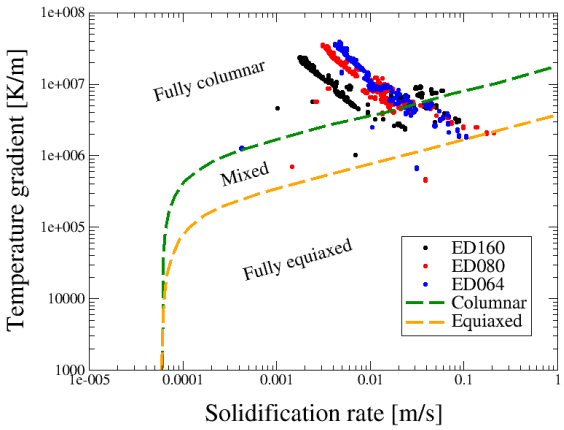

Fig. 6. Solidification map (G-R) for varying energy density.

The microstructure characteristics can also be assessed by plotting the temperature gradient (G) and dendritic growth velocity (also known as growth rate R) in the solidification map ($G - R$ diagram), as shown in Fig.6. The plot is based on the data extraction from the mushy region in the symmetry plane at quasi-steady state (marked by the colored dots). Such a region lies in the vicinity of the solidification boundary and is bounded by the solidus and liquidus temperature. Moreover, the analytically derived boundaries defining the columnar to equiaxed transition are also

mapped in Fig.6 (marked by the dashed lines), based on the CET formula (Gaumann et al., 2001) applied to Scalmalloy® (Singh et al., 2022). In the solidification map, the region above and to the left of the green dashed line is the region of high morphology factor (ratio of G to R), thus occupied by the fully columnar grains, whereas the region below and to the right of the yellow dashed line corresponds with the fully equiaxed grains (low morphology factor). The region between the dashed lines is the mixed zone, where the grain morphology is the mixture of both columnar and equiaxed. From the solidification map, it is found that the grains tend to be columnar for all process parameters used. However, there is a higher portion of the grains that lie in the mixed region and closer to the equiaxed region for ED080 and ED064, as compared with ED160. Therefore, low laser energy density has more tendency to yield equiaxed grains in the solidified regions rather than high energy density. Such finding is consistent with the observation of the cross-sectional morphology factor in Fig.5.

In the $G-R$ diagram, the top right region is associated with a high cooling rate (short solidification time), while the bottom-left corresponds with a low cooling rate (long solidification time). Fig. 6 thus suggests that the cooling rate (the product of G and R) increases with the laser scanning speed or is inversely proportional to the energy density. In general, cooling rate determines the grain size through the following relation (Kurz and Fisher, 1998):

$$\delta = at_f^n = b(CR)^{-n} \tag{27}$$

where δ is the secondary dendrite arm spacing, t_f local solidification time, CR the cooling rate, and a and b proportional constants that depend on the type of the alloy. With a long solidification time (low cooling rate) at low laser scanning speed, a sufficient time window is available for the formation of larger dendrite arm spacing and larger grains. Based on this relation, it can be inferred that the grain size generally increases with energy density or decreases with laser scanning speed. It must be underlined, though, that the Scalmalloy® composition in Singh et al. (2022) used for the CET boundaries in Fig.6 somewhat differs from that used in the current study. Therefore, a slight deviation of the boundaries is to be expected. However, given that the same relative positioning of the $G-R$ data plots predicted from simulations with varying energy densities would still apply otherwise, the interpretation would also still hold.

CONCLUSIONS

In this study, we employed a finite volume-based CFD model to simulate the thermo-fluid dynamics of the melt pool formed during Laser Powder Bed Fusion (LPBF) of Scalmalloy® components. The simulation results demonstrated that higher energy density, characterized by longer laser-material interaction time and more pronounced thermocapillary-driven convective flow, led to the formation of a wider and deeper melt pool. Through non-dimensional analysis, we assessed the relative importance of different driving forces in fluid flow and heat transfer, validating the assumptions used in the model. The findings revealed that the thermocapillary force (Marangoni effect) significantly dominated over thermal buoyancy and viscous effects in driving the flow. With Péclet numbers ranging from 10 to 15, it was evident that convective heat transfer plays a prominent role compared to conductive heat transfer. Thus, incorporating fluid flow prediction in the simulations, rather than relying entirely on heat conduction, is crucial for accurate results. The assumption of a flat surface used in this study was not fully justified, as the predicted Weber number is in the range of 7 – 10, thus requiring an appropriate model with free surface deformation. It should also be noted that the laminar flow assumption may be insufficient since the estimated Reynolds numbers fell within the turbulent regime for the melt pool flow. Therefore, future refinements of the simulations could involve turbulent flow modeling. To enhance the fidelity of the simulations, future work should also include temperature-dependent thermophysical properties obtained from experimental measurements of Scalmalloy® samples.

Furthermore, the microstructure prediction indicated that the maximum and average morphology factors increased with energy density, with high energy densities favoring the formation of columnar grains rather than equiaxed grains, as confirmed by the solidification map evaluation. Such tendency was caused by the increase in thermocapillary effect (represented by the Marangoni number), hence surface temperature gradient, as well as low cooling rates in the high energy density process. As the cooling rate intensified with higher laser scanning speeds, a decrease in grain size case could be inferred from the simulations.

ACKNOWLEDGMENT

This research was funded by Directorate of Research, Technology and Community Service of The Indonesia Ministry of Education, Culture, Research and Technology, grant number 410/LL3/AK.04/2022, 17 June 2022.

REFERENCES

Atthey, D. "A Mathematical Model for Fluid Flow in a Weld Pool at High Currents." *J. Fluid Mech.*, Vol. 98, No. 4, pp.787-801 (1980).

Barrionuevo, G. O., Ramos-Grez, J. A., Walczak, M., S´anchez-S´anchez, X., Guerra, C., Debut, A., Haro, E. "Microstructure Simulation and Experimental Evaluation of the Anisotropy of

316L Stainless Steel Manufactured by Laser Powder Bed Fusion." *Rapid Prototyp. J.*, Vol. 29, No. 3, pp.425-436 (2023).

Bayat, M., Mohanty, S., Hattel, J. H. "A Systematic Investigation of the Effects of Process Parameters on Heat and Fluid Flow and Metallurgical Conditions During Laser-Based Powder Bed Fusion of Ti6Al4V Alloy." *Int. J. Heat Mass Transf.*, Vol. 139, pp.213-230 (2019).

Bhat, C., Kumar, A., Lin, S. C., Jeng, J. Y. "Adaptive Mechanical Properties and Stretchability of Novel Chainmail Fabrics based on Overlapping Tessellation Strategies." *Addit. Manuf.*, Vol. 76, 103777 (2023).

Bhat, C., Kumar, A., Lin, S. C., Jeng, J. Y. "Design of Tessellation Based Load Transfer Mechanisms in Additively Manufactured Lattice Structures to Obtain Hybrid Responses". *Addit. Manuf.*, Vol. 76, 103774 (2023).

Blakey-Milner, B., Gradl, P., Snedden, G., Brooks, M., Pitot, J., Lopez, E., Leary, M., Berto, F., and du Plessis, A. "Metal Additive Manufacturing in Aerospace: A Review." *Mater. Des.*, Vol. 209, 110008 (2021).

Boley, C., Khairallah, S. A., Rubenchik, A. M. "Calculation of Laser Absorption by Metal Powders in Additive Manufacturing." *Appl. Opt*., Vol. 54, No. 9, pp.2477-2482 (2015).

Gaumann, M., Bezencon, C., Canalis, P., Kurz, W. "Single-Crystal Laser Deposition of Superalloys: Processing–Microstructure Maps." *Acta Mater.*, Vol. 49, No. 6, pp.1051-1062 (2001).

Gokuldoss, P. K., Kolla, S., and Eckert, J. "Additive Manufacturing Processes: Selective Laser Melting, Electron Beam Melting and Binder Jetting - Selection Guidelines." *Materials*, Vol. 10, No. 6, 672 (2017).

Huang, J.-Y., Chang, C.-H., Wang, W.-C., Chou, M.-J., Tseng, C.-C., and Tu, P.-W. "Systematic Evaluation of Selective Fusion Additive Manufacturing Based on Thermal Energy Source Applied in Processing of Titanium Alloy Specimens for Medical Applications." *Int. J. Adv. Manuf. Technol*., Vol. 109, No. 9, pp.2421-2429 (2020).

Khairallah, S. A., Anderson, A. T., Rubenchik, A., King, W. E. "Laser Powder-Bed Fusion Additive Manufacturing: Physics of Complex Melt Flow and Formation Mechanisms of Pores, Spatter, and Denudation Zones." *Acta Mater.*, Vol. 108, pp.36-45 (2016).

Khorasani, M., Ghasemi, A., Leary, M., Sharabian, E., Cordova, L., Gibson, I., Downing, D., Bateman, S., Brandt, M., Rolfe, B. "The Effect of Absorption Ratio on Melt Pool Features in Laser-Based Powder Bed Fusion of In718." *Opt. Laser Technol.*, Vol. 153, 108263 (2022).

Kuo, C. N., Peng, P. C., Liu, D. H., and Chao, C. Y., "Microstructure Evolution and Mechanical Property Response of 3D-Printed Scalmalloy with Different Heat-Treatment Times at 325° C", *Metals*, Vol. 11, No. 4, 555 (2021).

Kurz, W., and Fisher, D. *Fundamentals of Solidification*, 4th Ed., Trans Tech Publications, Switzerland (1998).

Lee, H. T., and Liu, T. C. "Microstructure and Intergranular Corrosion Resistance Evaluation of Alloy 82 Weldments." *J. Chin. Soc. Mech. Eng.*, Vol. 39, No. 2, pp.131-143 (2018).

Martucci, A., Aversa, A., Manfredi, D., Bondioli, F., Biamino, S., Ugues, D., Lombardi, M., Fino, P. "Low-Power Laser Powder Bed Fusion Processing of Scalmalloy®." *Materials*, Vol. 15, No. 9, 3123 (2022).

Parimi, L. L., Ravi, G., Clark, D., Attallah, M. M. "Microstructural and Texture Development in Direct Laser Fabricated In718." *Mater. Charact.*, Vol. 89, pp.102-111 (2014).

Raghavan, N., Dehoff, R., Pannala, S., Simunovic, S., Kirka, M., Turner, J., Carlson, N., Babu, S. S. "Numerical Modeling of Heat-Transfer and the Influence of Process Parameters on Tailoring the Grain Morphology of In718 in Electron Beam Additive Manufacturing." *Acta Mater.*, Vol. 112, pp.303-314 (2016).

Rahman, M. S., Schilling, P. J., Herrington, P. D., Chakravarty, U. K. "Heat Transfer and Melt-Pool Evolution During Powder-Bed Fusion of Ti-6Al-4V Parts Under Various Laser Irradiation Conditions." *ASME International Mechanical Engineering Congress and Exposition*, Vol. 84515, 2020, p. V004T04A017.

Shaikh, M. Q., Berfield, T. A., Atre, S. V. "Residual Stresses in Additively Manufactured Parts: Predictive Simulation and Experimental Verification." *Rapid Prototyp. J.*, Vol. 28, No. 10, pp.118-127 (2022).

Singh, A. K., Mundada, Y., Bajaj, P., Wilms, M. B., Patil, J. P., Mishra, S. K., Jägle, E. A., Arora, A. "Investigation of Temperature Distribution and Solidification Morphology in Multilayered Directed Energy Deposition of Al-0.5 Sc-0.5 Si Alloy." *Int. J. Heat Mass Transf.*, Vol. 186, 122492 (2022).

Sireesha, M., Lee, J., Kiran, A. S. K., Babu, V. J., Kee, B. B., and Ramakrishna, S. "A Review on Additive Manufacturing and Its Way into the Oil and Gas Industry." *RSC Adv.*, Vol. 8, No. 40, pp.22460-22468 (2018).

Spierings, A. B., Dawson, K., Voegtlin, M., Palm, F., Uggowitzer, P. J. "Microstructure and Mechanical Properties of As-Processed

Scandium-Modified Aluminium Using Selective Laser Melting." *CIRP Ann.*, Vol. 65, No. 1, pp.213-216 (2016).

Tan, J. H. K., Sing, S. L., Yeong, W. Y. "Microstructure Modelling for Metallic Additive Manufacturing: A Review." *Virtual Phys. Prototyp.*, Vol. 15, No. 1, pp.87-105 (2020).

Thangaraju, S., Heilmaier, M., Murty, B. S., Vadlamani, S. S. "On the Estimation of True Hall–Petch Constants and Their Role on the Superposition Law Exponent in Al Alloys." *Adv. Eng. Mater.*, Vol. 14, No. 10, pp.892-897 (2012).

Turangi, C., Haslich, F., Pasang, T. "An Investigation of the Influence of Changing Energy Volume Densities to Produce a Complete Process Parameter Window for Selective Laser Melting of Scalmalloy." *Nusantara Science and Technology Proceedings*, pp.21-33 (2020).

Vasco, J. C. "Additive Manufacturing for the Automotive Industry." In: Additive Manufacturing, pp.505-530 (2021).

Wang, D., Wei, X., Liu, J., Xiao, Y., Yang, Y., Liu, L., Tan, C., Yang, X., and Han, C. "Lightweight Design of an AlSi10Mg Aviation Control Stick Additively Manufactured by Laser Powder Bed Fusion." *Rapid Prototyp. J.*, Vol. 28, No. 10 (2022).

Wen, P., Voshage, M., Jauer, L., Chen, Y., Qin, Y., Poprawe, R., Schleifenbaum, J. H. "Laser Additive Manufacturing of Zn Metal Parts for Biodegradable Applications: Processing, Formation Quality and Mechanical Properties." *Mater. Des.*, Vol. 155, pp.36-45 (2018).

Wirth, F., Arpagaus, S., Wegener, K. "Analysis of Melt Pool Dynamics in Laser Cladding and Direct Metal Deposition by Automated High-Speed Camera Image Evaluation." *Addit. Manuf.*, Vol. 21, pp.369-382 (2018).

Ziolkowski, M., and Dyl, T. "Possible Applications of Additive Manufacturing Technologies in Shipbuilding: A Review." *Machines*, Vol. 8, No. 4, 84 (2020).

NOMENCLATURE

α liquid fraction

β thermal expansion coefficient

C velocity damping coefficient

C_p specific heat capacity

CR cooling rate

D_h hatch distance

$d\sigma/dT$ temperature gradient of surface tension

E_d energy density

ϵ a very small number to avoid division by zero

ε_r surface emissivity

F grain morphology factor

φ evaporation coefficient

$\vec{g}$ gravity acceleration vector

G temperature gradient

Gr Grashof number

H total enthalpy

h_c convective heat transfer coefficient

h_l laser penetration depth

η laser absorptivity by the metal powder

k thermal conductivity

k_B Boltzmann constant

L latent heat of fusion

L_v latent heat of vaporization

Ma Marangoni number

m_A atomic mass

μ dynamic viscosity

P laser power

Pe Péclet number

p pressure

p_{atm} atmospheric pressure

ϕ powder bed porosity

Re Reynolds number

r_l laser beam radius

ρ density

$\vec{S}_g$ momentum source term due to thermal buoyancy

S_H energy source term due to laser energy

$\vec{S}_m$ momentum source terms due to solidification

σ_B Stefan-Boltzmann constant

T temperature

T_b boiling temperature

T_l liquidus temperature

t_l powder layer thickness

T_{ref} reference temperature

T_s solidus temperature

$\vec{U}$ velocity vector

v_l laser scanning speed

We Weber number

x_i initial laser position x coordinate

y_i initial laser position y coordinate